International Journal of Heat and Mass Transfer 52 (2009) 4612–4623

Contents lists available at ScienceDirect

International Journal of Heat and Mass Transfer

journal homepage: www.elsevier.com/locate/ijhmt

Natural convection flows in porous trapezoidal enclosures with various inclination angles

Tanmay Basak [a], S. Roy [b], Amit Singh [b], A.R. Balakrishnan [a,*]

[a] Department of Chemical Engineering, Indian Institute of Technology Madras, Chennai 600036, India
[b] Department of Mathematics, Indian Institute of Technology Madras, Chennai 600036, India

ARTICLE INFO

Article history:
Received 14 May 2008
Received in revised form 19 January 2009
Accepted 22 January 2009
Available online 4 May 2009

Keywords:
Penalty finite element method
Natural convection
Porous medium
Trapezoidal cavity
Various angles
Uniform and non-uniform heating

ABSTRACT

Simulations were carried out using penalty finite element analysis with bi-quadratic elements to investigate the influence of uniform and non-uniform heating of bottom wall within a trapezoidal enclosure of various inclination angles (φ). Parametric study has been carried out for a wide range of Rayleigh number (Ra) ($10^3 \leqslant Ra \leqslant 10^6$), Prandtl number ($Pr$) ($0.026 \leqslant Pr \leqslant 988.24$) and Darcy number ($Da$) ($10^{-3} \leqslant Da \leqslant 10^{-5}$). Numerical results are presented in terms of stream functions, isotherm contours and Nusselt numbers. The heat transfer is primarily due to conduction at lower values of Darcy number (Da) and convection dominant heat transfer is observed at higher Da values. The intensity of circulation increases with increase in Darcy number. Increase in the intensity of circulations and larger temperature gradient are also observed with increase in φ from 0° to 45° especially at larger Pr and Ra. Non-uniform heating of the bottom wall produces greater heat transfer rate at the center of the bottom wall than uniform heating at all Rayleigh and Darcy numbers, but average Nusselt number is lower for non-uniform heating. Local heat transfer rates are found to be relatively greater for $\varphi = 0°$. It is observed that the local heat transfer rate at the central portion of bottom wall is larger for non-uniform heating case. Average Nusselt number plots show higher heat transfer rates at the bottom wall for $\varphi = 0°$ as compared to $\varphi = 45°$ and $\varphi = 30°$. It is observed that the average heat transfer rate at the bottom wall is found to be invariant with respect to φ at higher Ra for non-uniform heating. Critical Rayleigh numbers for conduction dominant heat transfer cases have been obtained and the power law correlations between average Nusselt number and Rayleigh numbers are presented for convection dominated regimes.

1. Introduction

The convective motion driven by buoyancy forces is well-known natural phenomena, and has attracted much attention [1–11]. The phenomena of natural convection in enclosures can be classified into two main groups – rectangular enclosures and non-rectangular enclosures. However, the number of studies on natural convection in porous non-rectangular geometries is very limited. In this context, buoyancy driven phenomena in porous media are actively under investigation. Natural convection flows are however particularly complex as they depend on several parameters among which the geometry and thermophysical characteristics of the fluid are the most important. Also, various applications depend on the product specification, shape of the container and heating characteristics. Numerical modeling offers a way to reduce expensive experiments. Most of the earlier modeling studies were carried out with conductive heating because of the simplicity of analytical and numerical solutions.

A significant amount of literature is available on the convection patterns in enclosures filled with porous media [12–15]. Natural convection in an enclosure filled with two layers of porous media was investigated numerically by Merrikh and Mohamad [16]. The focus of this work is on the validity of the Darcy model. Tong and Subramanian [17] and Lauriat and Prasad [18] considered Brinkman-extended Darcy model to examine the buoyancy effects on free convection in a vertical cavity. Brinkman-extended Darcy model has been introduced by Brinkman [19] in order to account for the transition from Darcy flow to highly viscous flow at high permeability values. However, Brinkman-extended Darcy model does not provide adequate description for the transition from the porous medium flow to pure fluid flow. A model that bridges the gap between the Darcy and Navier–Stokes equations is the Darcy–Forchheimer model developed by Vafai and Tien [20]. In addition, Darcy–Forchheimer model also describes the effect of inertia and viscous forces in the porous media and was used by Poulikakos and Bejan [21] and Lauriat and Prasad [22] to

* Corresponding author. Tel.: +91 0442257 4154; fax: +91 0442257 0509.
E-mail addresses: tanmay@iitm.ac.in (T. Basak), sjroy@iitm.ac.in (S. Roy), arbala@iitm.ac.in (A.R. Balakrishnan).

0017-9310/$ - see front matter © 2009 Elsevier Ltd. All rights reserved.
doi:10.1016/j.ijheatmasstransfer.2009.01.050

Nomenclature

Da	Darcy number
g	acceleration due to gravity, m s^{-2}
k	thermal conductivity, W m^{-1} K^{-1}
H	length/height of the trapezoidal cavity, m
N	total number of nodes
Nu	local Nusselt number
p	pressure, Pa
P	dimensionless pressure
Pr	Prandtl number
R	Residual of weak form
Ra	Rayleigh number
T	temperature, K
T_h	temperature of hot bottom wall, K
T_c	temperature of cold inclined wall, K
u	*x* component of velocity
U	*x* component of dimensionless velocity
v	*y* component of velocity
V	*y* component of dimensionless velocity
X	dimensionless distance along *x* coordinate
Y	dimensionless distance along *y* coordinate

Greek symbols

α	thermal diffusivity, m^2 s^{-1}
β	volume expansion coefficient, K^{-1}
γ	penalty parameter
θ	dimensionless temperature
ν	kinematic viscosity, m^2 s^{-1}
ρ	density, kg m^{-3}
Φ	basis functions
ψ	stream function
ξ	horizontal coordinate in a unit square
η	vertical coordinate in a unit square
φ	angle of inclination of side walls

Subscripts

b	bottom wall
l	left wall
r	right wall
s	side wall

investigate the natural convection in a vertical enclosure filled with a porous medium.

A few earlier works have been carried out on natural convection in complex porous geometries. Bortolozzi and Deiber [23] studied the two-field model for natural convection in porous media in relation to the one-field model, based on the assumption of local thermal equilibrium. These models are used to evaluate heat transfer through a porous medium of relatively high permeability contained in a vertical annulus. Numerical calculations are carried out for variable porosity and various correlations for the heat transfer coefficient between solid and fluid phases are analyzed. Badruddin et al. [24] have studied the steady state heat transfer in a porous medium fixed in a vertical annular cylinder. The Darcy model of flow was employed and heat transfer was assumed to take place by natural convection and radiation. The governing equations were solved using the finite element method. They found that if interphase heat transfer coefficient and modified conductivity ratio are maintained at high values, then thermal equilibrium is approached with both solid and fluid phases having similar temperatures.

A few recent works are also based on various complex situations in porous medium [25–27]. The effect of viscous dissipation has been considered for Darcy model by Saeid and Pop [25]. Their studies show that the viscous dissipation effect reduces the heat transfer rate and the average Nusselt number in porous cavity decreases with the increase of the viscous dissipation parameter. Recently, Basak et al. [26] studied numerically the natural convection flows in a square cavity filled with a porous matrix for various boundary conditions and wide range of parameters. Results showed that non-uniform heating of the bottom wall produces greater heat transfer rate at the center of the bottom wall than uniform heating case for all *Ra*, but average *Nu* shows overall lower heat transfer rates for non-uniform heating case.

Baytas and Pop [27] have studied natural convection on trapezoidal porous enclosure with situations such as top enclosure being cooled, bottom surface being heated and the remaining two non-parallel plane sidewalls of the enclosure being adiabatic. Although their study deals with heat transfer analysis on various application in trapezoidal porous spaces, a comprehensive analysis on heat transfer and flow circulations for applications on extraction of molten metals, salt water and olive oil confined within a porous bed is yet to appear in literature for various tilt angles.

The objective of the present study is to investigate the circulation and temperature distributions in various enclosures (trapezoidal or square) with uniformly and non-uniformly heated bottom plate and cooled side walls. The effect of geometry has been illustrated for various angle of the sidewall varying within 0–45°. The analysis has been carried out for various materials with a range of Prandtl number (*Pr*), e.g., molten metals ($Pr = 0.004—0.026$), gases ($Pr = 0.7—1$), salt water ($Pr = 1.7—13.7$), oils ($Pr = 50—10^3$), etc. whereas earlier literature primarily involve air and water only. The thermal processing of various materials within a porous enclosure is quite important especially for separation or extraction purposes. The motivation of this study is to analyze the practical situation where the vertical wall is at ambient temperatures and inside temperature is maintained high using any heating system, while the top wall is insulated. The boundary conditions due to uniform heating correspond to jump discontinuities at corner points and similar boundary conditions were also used in earlier works on natural convection in square cavities [5,26]. The boundary condition due to non-uniform heating has been represented by sinusoidal distribution of temperature and this type of boundary condition is particularly useful for processing molten glass [28].

The geometry of the trapezoidal enclosure with boundary conditions is shown in Fig. 1a–c. In the current study, the Galerkin finite element method is used with penalty parameter to solve the non-linear coupled partial differential equations governing flow and temperature fields for both uniform and non-uniform heating of the bottom wall. The Darcy–Forchheimer model without the Forchheimer's inertia term has been adopted. The jump discontinuities in Dirichlet type of wall boundary conditions at the corner points correspond to computational singularities. In particular, the singularities at the bottom corner nodes need special attention. Non-orthogonal grid generation has been done with iso-parametric mapping [29,30]. An overview on grid generation using iso-parametric mapping is given in Appendix A. The Galerkin finite element with iso-parametric mapping has been used based on the fact that automatically generated grid in a pseudo-square domain makes the method robust for any complex geometry. Numerical results are obtained to describe the circulation and temperature distributions within the domain and the heat transfer rate for both the walls in terms of local and average Nusselt numbers. Local and

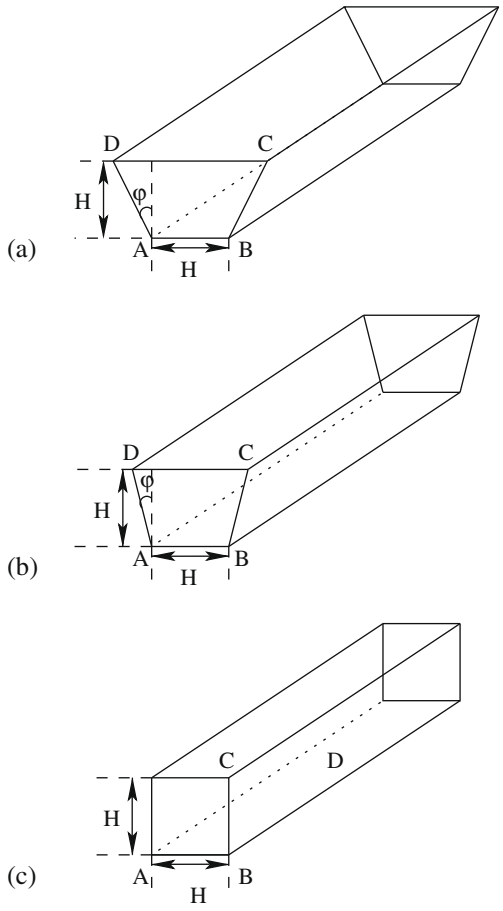

Fig. 1. Schematic diagram of the physical system for (a) $\varphi = 45^\circ$, (b) $\varphi = 30^\circ$ and (c) $\varphi = 0^\circ$.

average Nusselt numbers have been evaluated using bi-quadratic basis functions. The heat transfer effects have been illustrated based on two cases: uniformly heated bottom wall and non-uniformly heated bottom wall.

2. Mathematical formulation

Consider a trapezoidal cavity, filled with a porous medium, with the left wall inclined at an angle $\varphi = 45^\circ, 30^\circ$ and 0° with the y-axis as seen in Fig. 1a, b and c, respectively. Thermophysical properties of the fluid in the flow field are assumed to be constant except the density variations causing a body force term in the momentum equation. The Boussinesq approximation is invoked the variation of fluid density with temperature and to couple in this way the temperature field to the flow field. Further, it is assumed that the temperature of the fluid phase is equal to the temperature of the solid phase everywhere in the porous region and local thermal equilibrium (LTE) is applicable in the present investigation [13]. Also, a velocity square term could be incorporated in the momentum equations to model the inertia effect which is more important for non-Darcy convective boundary layer flow over the surface of a body embedded in a high porosity media. However, this term has been neglected in the present study because this study involves the natural convection flow in a cavity filled with a porous medium. Under these assumptions and following the earlier works [20,4] with the Forchheimer's inertia term being neglected, the governing equations for steady two-dimensional natural convection flow in the porous cavity using conservation of mass, momentum and energy in dimensionless form can be written as:

$$\frac{\partial U}{\partial X} + \frac{\partial V}{\partial Y} = 0 \tag{1}$$

$$U\frac{\partial U}{\partial X} + V\frac{\partial U}{\partial Y} = -\frac{\partial P}{\partial X} + Pr\left(\frac{\partial^2 U}{\partial X^2} + \frac{\partial^2 U}{\partial Y^2}\right) - \frac{Pr}{Da}U \tag{2}$$

$$U\frac{\partial V}{\partial X} + V\frac{\partial V}{\partial Y} = -\frac{\partial P}{\partial Y} + Pr\left(\frac{\partial^2 V}{\partial X^2} + \frac{\partial^2 V}{\partial Y^2}\right) - \frac{Pr}{Da}V + RaPr\theta \tag{3}$$

$$U\frac{\partial \theta}{\partial X} + V\frac{\partial \theta}{\partial Y} = \frac{\partial^2 \theta}{\partial X^2} + \frac{\partial^2 \theta}{\partial Y^2} \tag{4}$$

where

$$X = \frac{x}{H}, \quad Y = \frac{y}{H}, \quad U = \frac{uH}{\alpha}, \quad V = \frac{vH}{\alpha}, \quad \theta = \frac{T - T_c}{T_h - T_c}$$
$$P = \frac{pH^2}{\rho\alpha^2}, \quad Pr = \frac{\nu}{\alpha}, \quad Da = \frac{K}{H^2}, \quad Ra = \frac{g\beta(T_h - T_c)H^3}{\nu\alpha} \tag{5}$$

The dimensionless form of the boundary conditions are:

$$U = 0, \ V = 0, \ \theta = 1, \ \text{or} \ \theta = sin(\pi X), \forall Y = 0, \ 0 \leqslant X \leqslant 1$$
$$U = 0, \ V = 0, \ \theta = 0, \quad \forall X cos(\varphi) + Y sin(\varphi) = 0, 0 \leqslant Y \leqslant 1$$
$$U = 0, \ V = 0, \ \theta = 0, \quad \forall X cos(\varphi) - Y sin(\varphi) = cos(\varphi), 0 \leqslant Y \leqslant 1$$
$$U = 0, \ V = 0, \ \frac{\partial \theta}{\partial Y} = 0, \quad \forall Y = 1, -tan(\varphi) \leqslant X \leqslant 1 + tan(\varphi). \tag{6}$$

3. Solution procedure

The momentum and energy balance equations (Eqs. (2)–(4)) are solved using the Galerkin finite element method. The continuity equation (Eq. (1)) is used as a constraint due to mass conservation and this constraint may be used to obtain the pressure distribution. In order to solve Eqs. (2) and (3), the penalty finite element method is used where the pressure P is eliminated by a penalty parameter γ and the incompressibility criteria given by Eq. (1) results in

$$P = -\gamma\left(\frac{\partial U}{\partial X} + \frac{\partial V}{\partial Y}\right) \tag{7}$$

The continuity equation (Eq. (1)) is automatically satisfied for large values of γ. Typical values of γ that yield consistent solutions are 10^7. Using Eq. (7), the momentum balance equations (Eqs. (2) and (3)) reduce to

$$U\frac{\partial U}{\partial X} + V\frac{\partial U}{\partial Y} = \gamma\frac{\partial}{\partial X}\left(\frac{\partial U}{\partial X} + \frac{\partial V}{\partial Y}\right) + Pr\left(\frac{\partial^2 U}{\partial X^2} + \frac{\partial^2 U}{\partial Y^2}\right) - \frac{Pr}{Da}U \tag{8}$$

and

$$U\frac{\partial V}{\partial X} + V\frac{\partial V}{\partial Y} = \gamma\frac{\partial}{\partial Y}\left(\frac{\partial U}{\partial X} + \frac{\partial V}{\partial Y}\right) + Pr\left(\frac{\partial^2 V}{\partial X^2} + \frac{\partial^2 V}{\partial Y^2}\right) - \frac{Pr}{Da}V + RaPr\theta \tag{9}$$

The system of equations (Eqs. (4), (8) and (9)) with boundary conditions (Eq. (6)) are solved using Galerkin finite element method [29]. Since the solution procedure is explained in an earlier work [26], the detailed description is not included in this paper. The numerical solutions are obtained in terms of the velocity components (U, V) and stream function (ψ) is evaluated using the relationship between the stream function (ψ) and the velocity components [31], where the stream function (ψ) is defined in the usual way as $U = \frac{\partial \psi}{\partial Y}$ and $V = -\frac{\partial \psi}{\partial X}$. It may be noted that, the positive sign of ψ denotes anti-clockwise circulation and the clockwise circulation is represented by the negative sign of ψ. The no-slip condition is valid at all boundaries as there is no cross flow, hence $\psi = 0$ at the boundaries. For steady flow, stream lines are equivalent to the paths followed by the individual particles in the fluid.

The heat transfer coefficient in terms of the local Nusselt number (Nu) is defined by

$$Nu = -\frac{\partial\theta}{\partial n} \tag{10}$$

where n denotes the normal direction on a plane. The local Nusselt numbers at bottom wall (Nu_b), left wall (Nu_l) and right wall (Nu_r) are defined as

$$Nu_b = \sum_{i=1}^{9} \theta_i \frac{\partial \Phi_i}{\partial Y} \tag{11}$$

$$Nu_l = \sum_{i=1}^{9} \theta_i \left(cos\varphi \frac{\partial \Phi_i}{\partial X} + sin\varphi \frac{\partial \Phi_i}{\partial Y} \right) \tag{12}$$

and

$$Nu_r = -\sum_{i=1}^{9} \theta_i \left(cos\varphi \frac{\partial \Phi_i}{\partial X} - sin\varphi \frac{\partial \Phi_i}{\partial Y} \right) \tag{13}$$

The average Nusselt numbers at the bottom, left and right walls are

$$\overline{Nu_b} = \frac{\int_0^1 Nu_b dX}{X|_0^1} = \int_0^1 Nu_b dX \tag{14}$$

$$\overline{Nu_l} = cos\varphi \int_0^{\frac{1}{cos\varphi}} Nu_l ds_1 \tag{15}$$

and

$$\overline{Nu_r} = cos\varphi \int_0^{\frac{1}{cos\varphi}} Nu_r ds_2 \tag{16}$$

where ds_1, ds_2 is the small elemental lengths along the left and right walls, respectively.

4. Results and discussion

4.1. Numerical tests

The grid generation has been carried out by iso-parametric mapping and the detailed explanation is given in Appendix A. The computational domain consists of 20×20 bi-quadratic elements which correspond to 41×41 grid points in ξ–η domain as seen in Fig. 2. The bi-quadratic elements with lesser number of nodes smoothly capture the non-linear variations of the field variables which are in contrast with finite difference solutions available in the literature [27]. In order to assess the accuracy of the numerical procedure, the algorithm has been benchmarked based on the grid size for the fluid filled trapezoidal cavity [32]. Further, the result is in agreement with an earlier work [22] for porous square enclosure with heated side wall.

Numerical solutions are obtained for $Ra = 10^3$–$10^6, Pr = 0.026$–988.24 and $Da = 10^{-5}$–10^{-3} with uniform and non-uniform heating of the bottom wall where two vertical walls are cooled and the top wall is well insulated. The jump discontinuity in Dirichlet type of boundary conditions at the corner point on the bottom wall (see Fig. 1) corresponds to computational singularity. To ensure the convergence of the numerical solution to the exact solution, the grid sizes have been optimized and the results presented here are independent of grid sizes. In particular, the singularity at the corner nodes of the bottom wall needs special attention. The grid size dependent effect of the temperature discontinuity at the corner points on the local (and the overall) Nusselt numbers tend to increase as the mesh spacing at the corner is reduced. One of the ways for handling the problem is assuming the average temperature of the two walls at the corner and keeping the adjacent grid-nodes at the respective wall temperatures. However, according to earlier work by Ganzarolli and Milanez [33], this procedure is still grid dependent unless a sufficiently refined mesh is implemented. Hence, once any corner formed by the intersection of two differently heated boundary walls is assumed at the average temperature of the adjacent walls, the optimal grid size obtained for each configuration corresponds to the mesh spacing over which further grid refinements lead to grid invariant results in both heat transfer rates and flow fields.

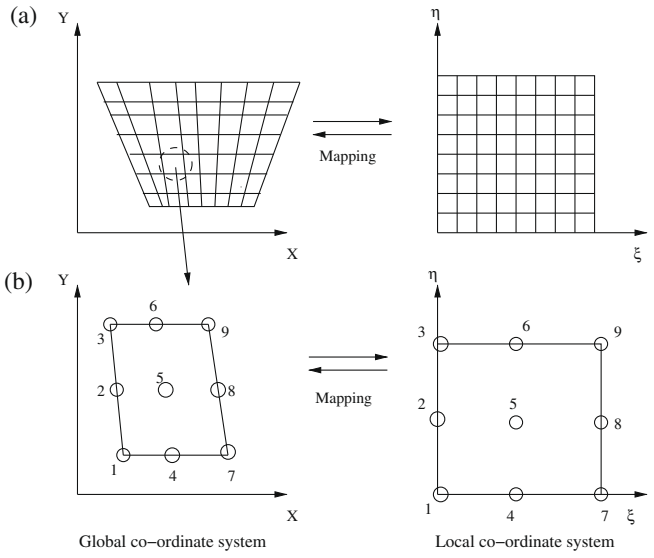

Fig. 2. (a) The mapping of trapezoidal domain to a square domain in ξ–η coordinate system and (b) the mapping of an individual element to a single element in ξ–η coordinate system.

In the current investigation, Gaussian quadrature based finite element method provides the smooth solutions at the interior domain including the corner regions as evaluation of residuals depends on interior Gauss points and thus the effect of corner nodes is less pronounced in the final solution. The present finite element approach offers special advantages on evaluation of local Nusselt number at the bottom and side walls as the element basis functions are used to evaluate the heat flux.

4.2. Effects of Darcy number: uniform heating at bottom wall

Figs. 3–7 illustrate the stream function and isotherm contours for various $Ra = 10^3$–$10^6, Da = 10^{-5}$–10^{-3} and $Pr = 0.026$ (molten metal), 7.2 (salt water) and 988.24 (olive oil) when the bottom wall is uniformly heated and the side walls are cooled while the top wall is well insulated. Due to the hot bottom wall, the fluid near that wall is hotter than the fluid near the cold wall and hence fluid near the hot bottom wall have lower density than that near the vertical wall. As a result, fluid moves upward from the middle portion of the bottom wall and flows down along the two cold side walls resulting in oppositely rotating circulations inside the cavity. Results indicate that the streamlines and isotherms are strongly dependent on Darcy number.

Fig. 3 displays the temperature and stream function contours for $Da = 10^{-5}$ and $Ra = 10^6$ with $Pr = 7.2$. In this case, the flow is seen to be very weak as observed from the stream function contours. The temperature contours are smooth and monotonic and this indicates that heat transfer is primarily due to conduction. Isotherms with $\theta = 0.1$–0.4 occur symmetrically near the side walls of the enclosure for $\varphi = 45^\circ$ (Fig. 3a). The other temperature contours with $\theta \geqslant 0.5$ are smooth curves symmetric with respect to vertical symmetrical line at the center. For $\varphi = 30^\circ$, the isotherms with $\theta = 0.1$–0.3 occur symmetrically near the side walls of the

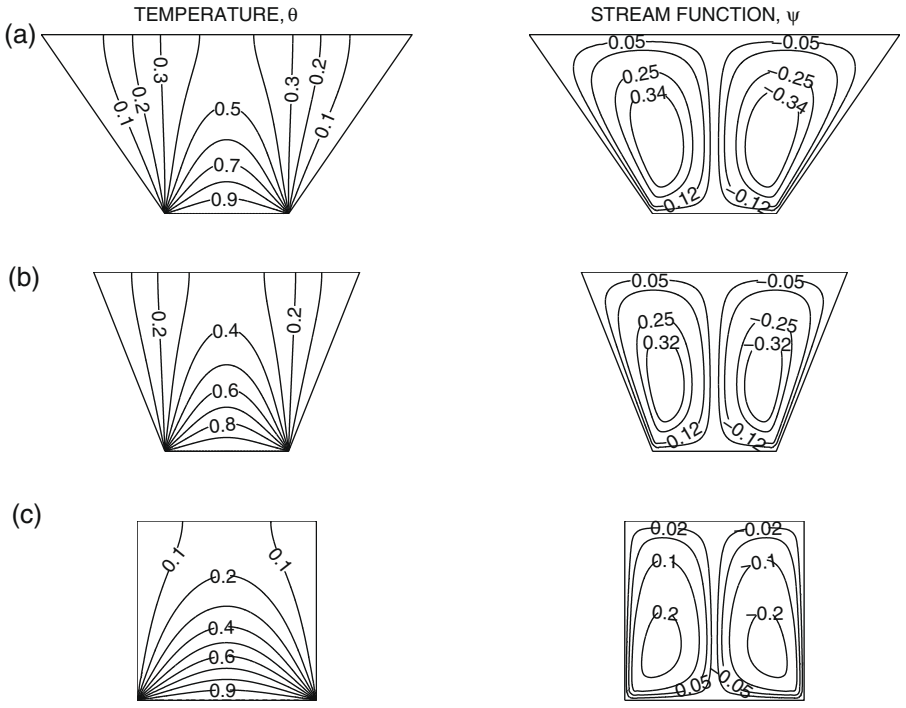

Fig. 3. Contour plots for uniform bottom heating, $\theta(X,0)=1$, with $Pr=7.2$ (salt water), $Ra=10^6$ and $Da=10^{-5}$ for (a) $\varphi=45^\circ$, (b) $\varphi=30^\circ$ and (c) $\varphi=0^\circ$. Clockwise and anti-clockwise flows are shown via negative and positive signs of stream function, respectively.

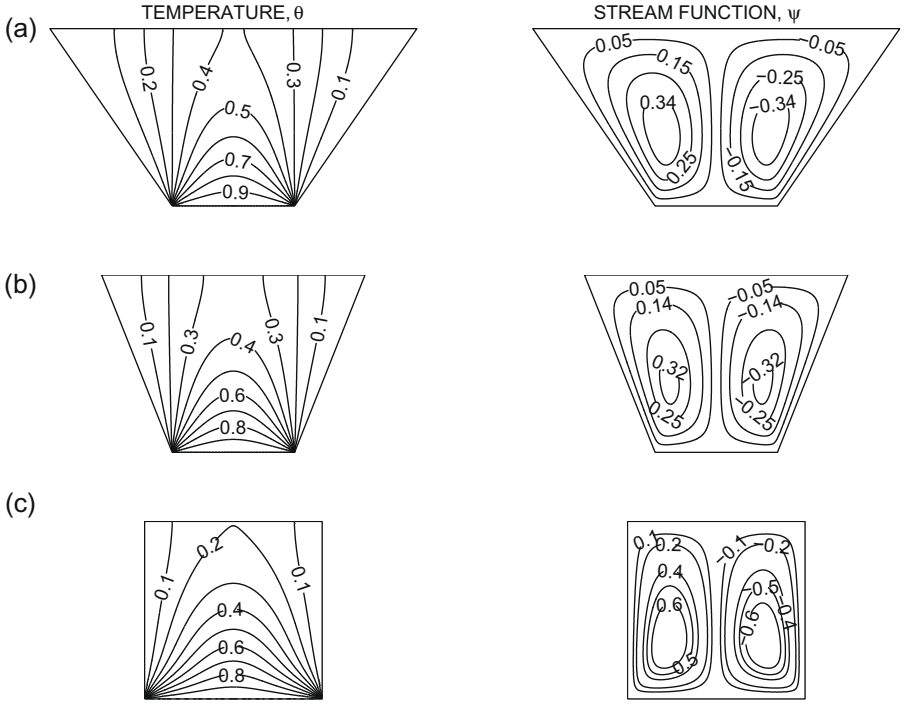

Fig. 4. Contour plots for uniform bottom heating, $\theta(X,0)=1$, with $Pr=7.2$ (salt water) and $Da=10^{-3}$ for (a) $\varphi=45^\circ; Ra=10^4$, (b) $\varphi=30^\circ; Ra=10^4$ and (c) $\varphi=0^\circ; Ra=3\times10^4$. Clockwise and anti-clockwise flows are shown via negative and positive signs of stream function, respectively.

enclosure (Fig. 3b) whereas $\theta \geqslant 0.4$ are smooth curves symmetric with respect to vertical symmetric line. For square cavity $(\varphi=0^\circ), \theta=0.1$ is symmetric along the side walls and $\theta \geqslant 0.2$ are smooth curves symmetric with respect to the central symmetric line (Fig. 3c). Increase in the intensity of circulations and larger temperature gradient are observed with increase in φ from 0° to 45°.

During conduction dominant heat transfer, the temperature profiles are almost invariant with respect to *Ra* and it is observed that the significant convection is initiated corresponding to a critical *Ra*. The critical Rayleigh number for the conduction dominant mode is found as $Ra=10^4$ for $\varphi=45^\circ, 30^\circ$ and $Ra=3\times10^4$ for $\varphi=0^\circ$ with $Da=10^{-3}$ and $Pr=7.2$. At critical *Ra*, the distortion of the isotherm gradually increases and convection becomes

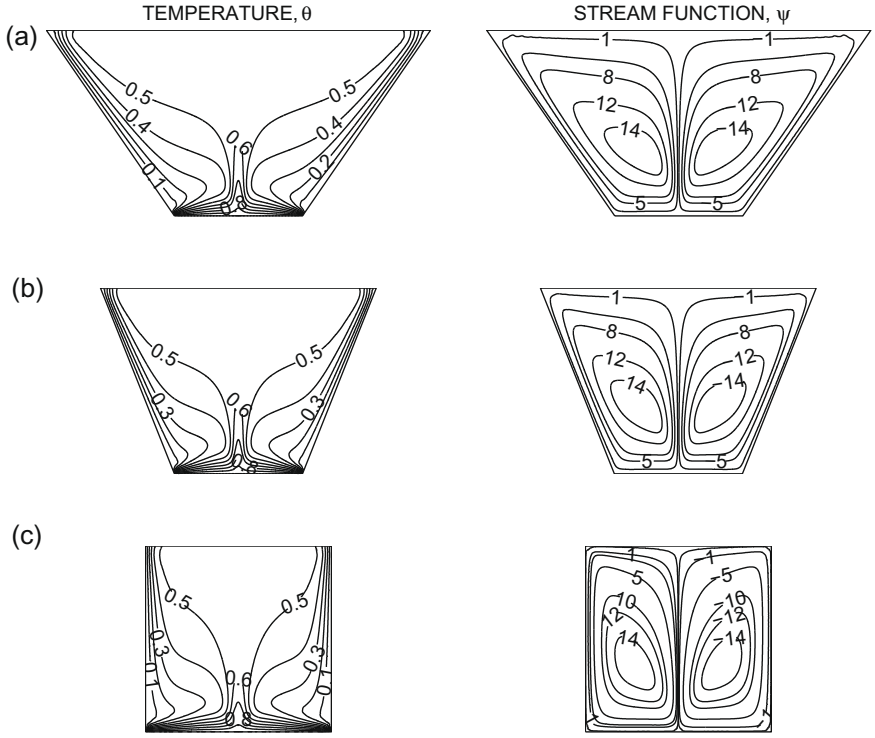

Fig. 5. Contour plots for uniform bottom heating, $\theta(X,0)=1$, with $Pr=7.2$ (salt water), $Ra=10^6$ and $Da=10^{-3}$ for (a) $\varphi=45^\circ$, (b) $\varphi=30^\circ$ and (c) $\varphi=0^\circ$. Clockwise and anti-clockwise flows are shown via negative and positive signs of stream function, respectively.

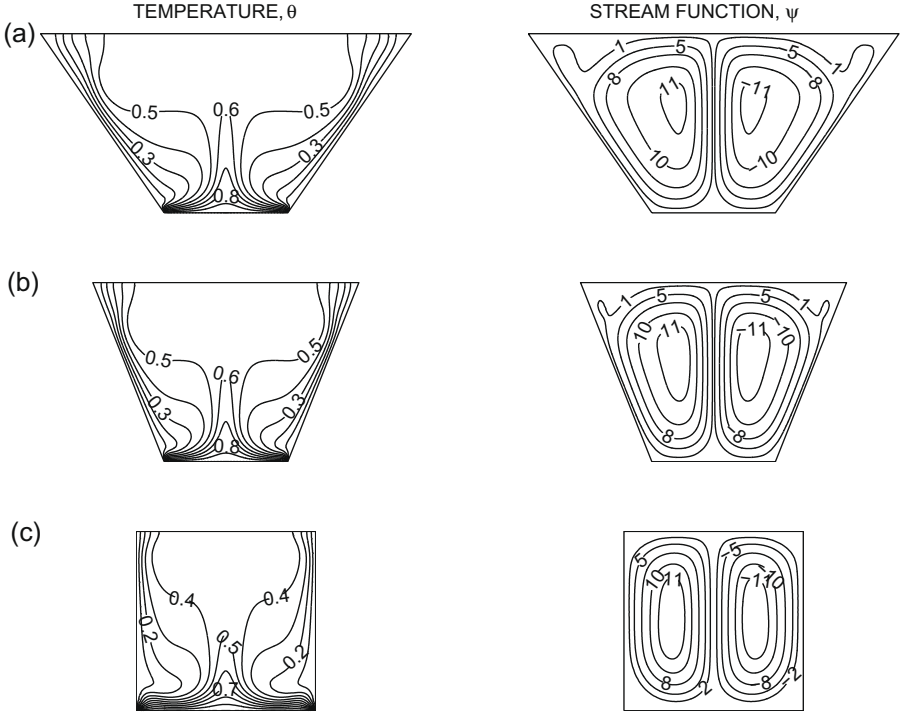

Fig. 6. Contour plots for uniform bottom heating, $\theta(X,0)=1$, with $Pr=0.026$ (molten metal), $Ra=10^6$ and $Da=10^{-3}$ for (a) $\varphi=45^\circ$, (b) $\varphi=30^\circ$ and (c) $\varphi=0^\circ$. Clockwise and anti-clockwise flows are shown via negative and positive signs of stream function, respectively.

dominant mode of heat transfer as seen in Fig. 4a–c. At the onset of convection, the isotherms gradually get distorted and move towards the walls. The value of critical *Ra* has been obtained from asymptotes of average Nusselt number vs Rayleigh number plot as discussed later.

It is observed that the flow is strongly dependent on *Ra* for $Da=10^{-3}$. For $Da=10^{-3}, Ra=10^6$ and $Pr=7.2$, the circulation near the central regimes are stronger and consequently, the temperature contours with $\theta \leqslant 0.5$ irrespective of φ's start getting shifted towards the side walls and they break into two symmetric

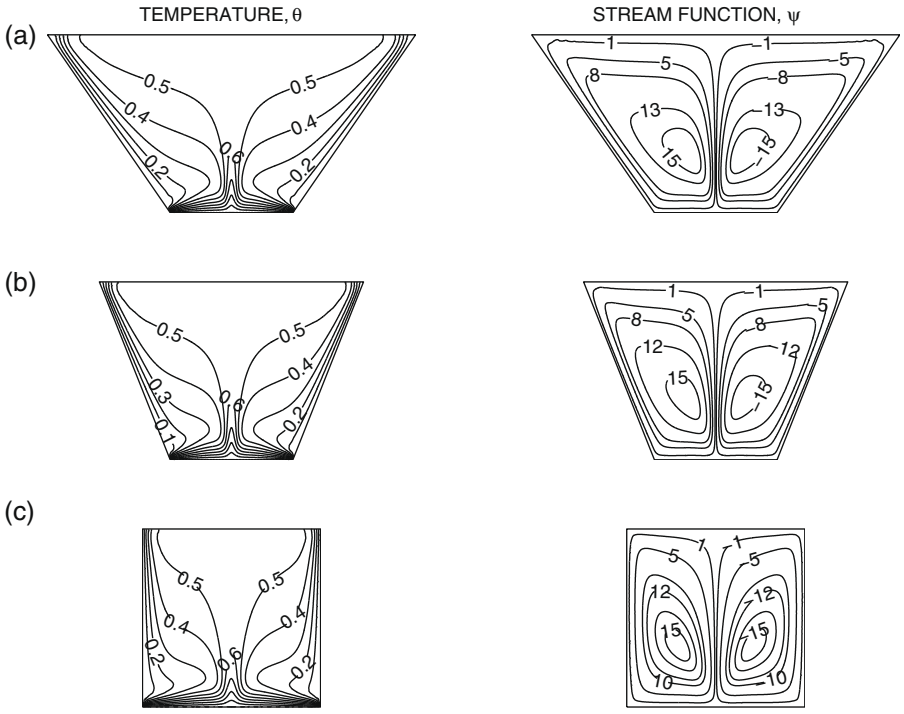

Fig. 7. Contour plots for uniform bottom heating, $\theta(X,0)=1$, with $Pr=988.24$ (olive oil), $Ra=10^6$ and $Da=10^{-3}$ for (a) $\varphi=45^\circ$, (b) $\varphi=30^\circ$ and (c) $\varphi=0^\circ$. Clockwise and anti-clockwise flows are shown via negative and positive signs of stream function, respectively.

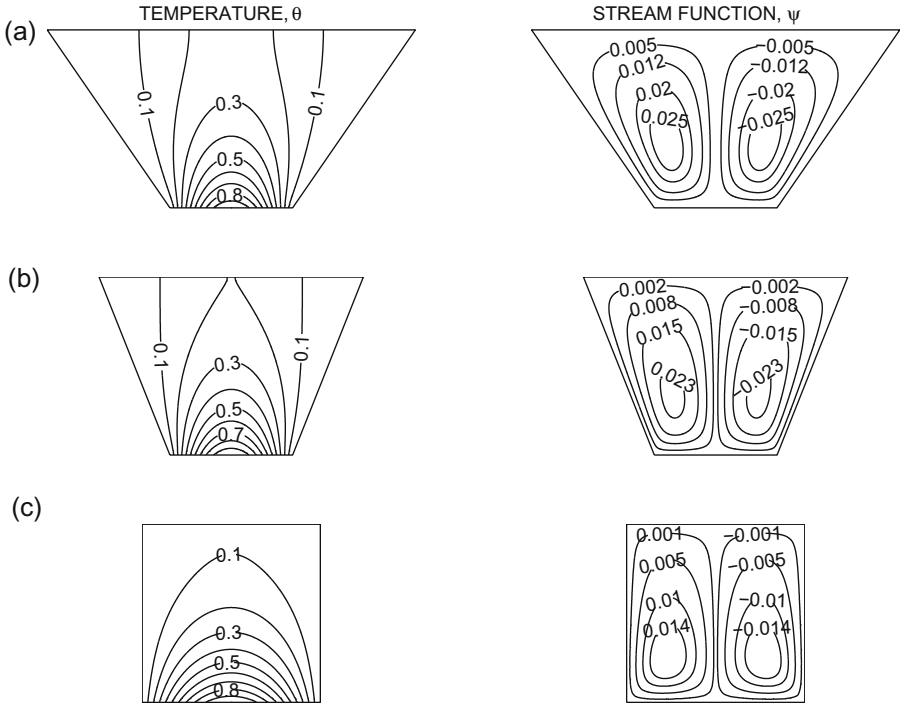

Fig. 8. Contour plots for non-uniform bottom heating, $\theta(X,0)=\sin(\pi X)$, with $Pr=7.2$ (salt water), $Ra=10^3$ and $Da=10^{-3}$ for (a) $\varphi=45^\circ$, (b) $\varphi=30^\circ$ and (c) $\varphi=0^\circ$. Clockwise and anti-clockwise flows are shown via negative and positive signs of stream function, respectively.

contour lines (see Fig. 5). The presence of significant convection is also exhibited in isotherms which start getting deformed and pushed towards the side walls. The intensity of flow circulations for $Da=10^{-3}$ is represented with $|\psi|_{max}=14$ irrespective of φ's and the intensity is significantly greater than that at $Da=10^{-5}$ which corresponds to $|\psi|_{max}=0.34$ for $\varphi=45^\circ$, $|\psi_{max}|=0.32$ for $\varphi=30^\circ$ and $|\psi_{max}|=0.2$ for $\varphi=0^\circ$. The greater circulation in each half of the box follows a progressive wrapping around the centers of rotation, and a more pronounced compression of isotherms towards the boundary surfaces of the enclosures occur. Consequently, the formation of thermal boundary layers is observed at the side walls as well as at the bottom wall whereas small temper-

ature gradients are present from the central core towards the top half of the cavity.

Comparative study for two limits of Prandtl numbers is shown in Figs. 6 and 7. At $Ra = 10^6$ for $Pr = 0.026$ and $Da = 10^{-3}$ (Fig. 6), the isotherm contours are less compressed towards the side and bottom walls forming weaker temperature gradient within the thermal boundary layer. Hence, the thicknesses of the thermal boundary layers are greater for $Pr = 0.026$ as compared to $Pr = 7.2$. For $Pr = 988.24$ at $Ra = 10^6$ (Fig. 7), temperature contours along the walls are highly compressed and thickness of the thermal boundary layer is reduced. The intensity of flow circulations for $Pr = 988.24$ is represented with $|\psi|_{max} = 15$ whereas it is observed

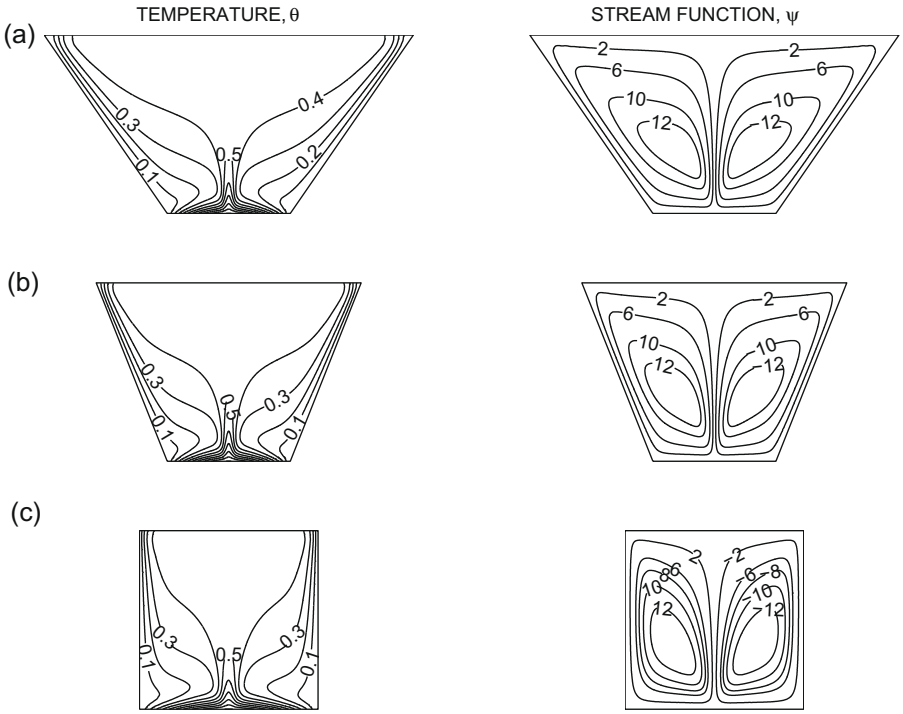

Fig. 9. Contour plots for non-uniform bottom heating, $\theta(X,0) = \sin(\pi X)$, with $Pr = 7.2$ (salt water), $Ra = 10^6$ and $Da = 10^{-3}$ for (a) $\varphi = 45^\circ$, (b) $\varphi = 30^\circ$ and (c) $\varphi = 0^\circ$. Clockwise and anti-clockwise flows are shown via negative and positive signs of stream function, respectively.

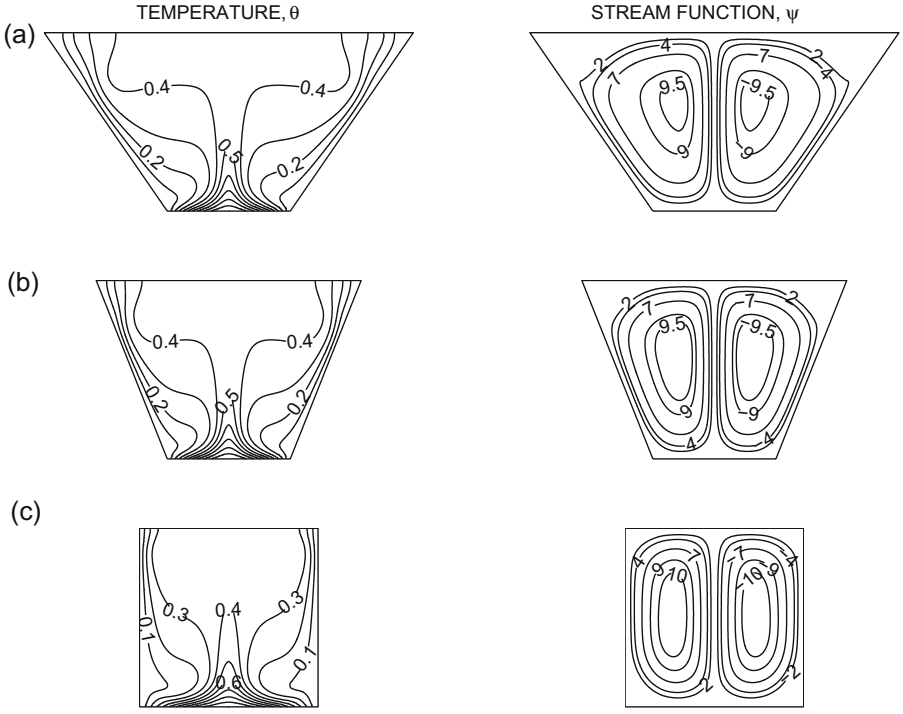

Fig. 10. Contour plots for non-uniform bottom heating, $\theta(X,0) = \sin(\pi X)$, with $Pr = 0.026$ (molten metal), $Ra = 10^6$ and $Da = 10^{-3}$ for (a) $\varphi = 45^\circ$, (b) $\varphi = 30^\circ$ and (c) $\varphi = 0^\circ$. Clockwise and anti-clockwise flows are shown via negative and positive signs of stream function, respectively.

that $|\psi|_{max} = 11$ for $Pr = 0.026$ and $|\psi|_{max} = 14$ for $Pr = 7.2$ for all tilt angles. These values further illustrate higher intensity of convection with higher Prandtl numbers. It may also be remarked that the larger intensity of circulations for higher Pr fluid causes the shapes of stream functions almost trapezoidal near the walls and that signifies enhanced mixing effects.

4.3. Effects of Darcy number: non-uniform heating at bottom wall

Figs. 8–11 show the effects for $Ra = 10^3$–10^6, $Da = 10^{-5}$–10^{-3} and $Pr = 0.026$–988.24 when the bottom wall is non-uniformly heated following sinusoidal variation. As seen in Figs. 3–7, uniform heating of bottom wall causes a finite discontinuity in Dirichlet type boundary conditions for the temperature distribution at both edges of the bottom wall. In contrast, the non-uniform heating removes the singularity at the edges of bottom wall and provides a smooth temperature distribution in the entire cavity. For $Da = 10^{-5}$, $Ra = 10^6$ and $Pr = 7.2$, the isotherms (figure not shown) are similar to that with uniform heating case as seen in Fig. 3 and hence the heat transfer is primarily due to conduction. It may be noted that the temperature at the bottom wall is non-uniform and the maximum in temperature occurs at the center. Thus, heat transfer rate is maximum at the center and the detailed analysis is illustrated in the following section.

During conduction dominant mode ($Ra = 10^3$) for $Pr = 7.2$ and $Da = 10^{-3}$ with $\varphi = 45^\circ$, the temperature contours with $\theta = 0.1$–0.2 occur symmetrically near the side walls of the enclosure as seen in Fig. 8a whereas the contours with $\theta \leqslant 0.3$ was found to occur symmetrically near the side walls for uniform heating case (figure not shown). Similarly for $\varphi = 30^\circ$, temperature contours with $\theta = 0.1 - 0.2$ occur symmetrically near the side walls of the enclosure (Fig. 8b). In contrast, for $\varphi = 0^\circ$, temperature contours are smooth curves symmetric with respect to the vertical symmetric line (Fig. 8c). It is observed that the significant convection for $Pr = 7.2$ and $Da = 10^{-3}$, is initiated at critical $Ra = 2 \times 10^4$ for $\varphi = 45^\circ$ and 30° and $Ra = 3 \times 10^4$ for $\varphi = 0^\circ$ (figure not shown).

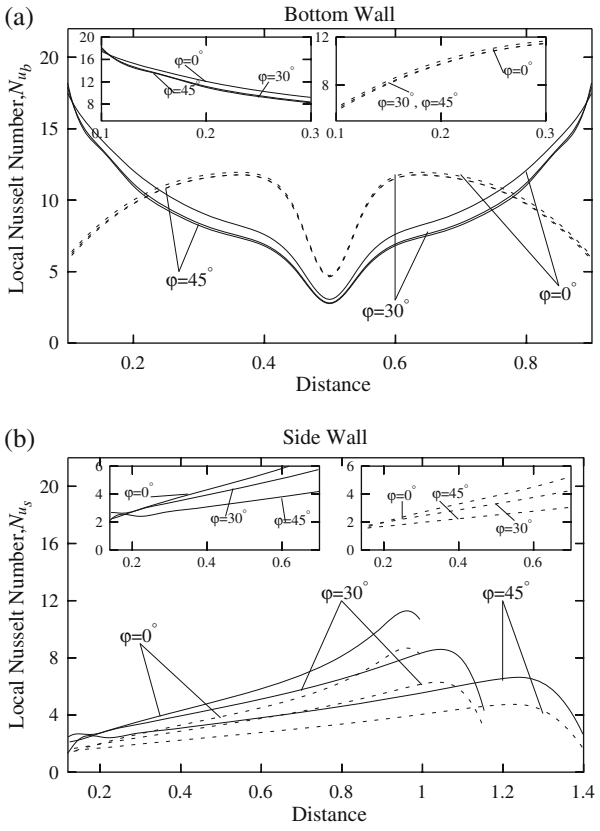

Fig. 12. Variation of local Nusselt number with distance involving $Pr = 7.2$ (salt water), $Da = 10^{-3}$ and $Ra = 10^6$ for (a) the bottom wall, (b) the side wall in presence of uniform heating (—) and non-uniform heating (- - -) cases. Inset plots show heat transfer rates for selected regimes with uniform heating (—) and non-uniform heating (- - -).

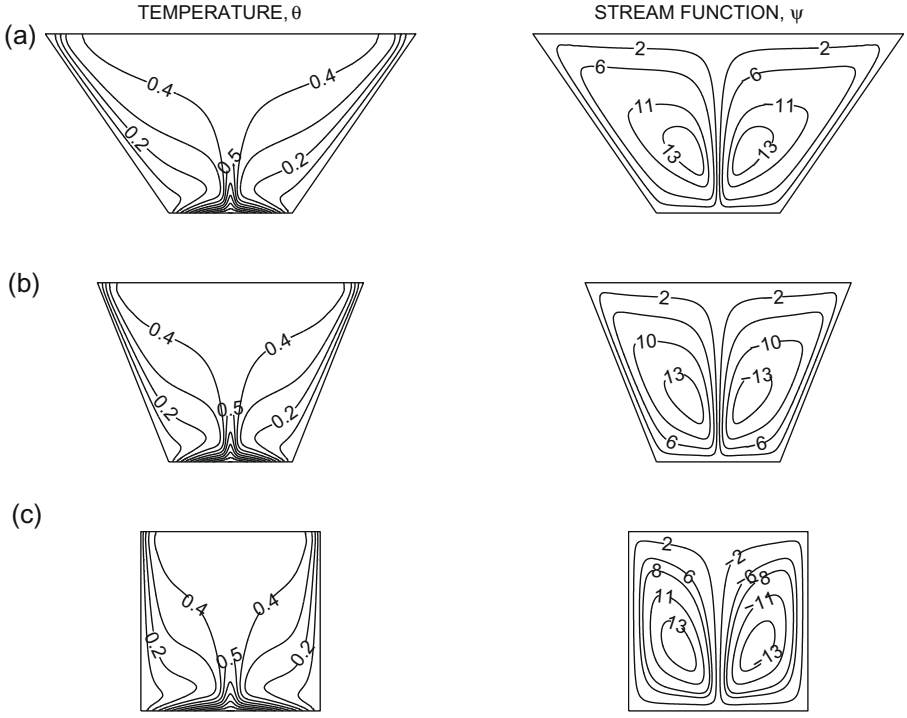

Fig. 11. Contour plots for non-uniform bottom heating, $\theta(X, 0) = \sin(\pi X)$, with $Pr = 988.24$ (olive oil), $Ra = 10^6$ and $Da = 10^{-3}$ for (a) $\varphi = 45^\circ$, (b) $\varphi = 30^\circ$ and (c) $\varphi = 0^\circ$. Clockwise and anti-clockwise flows are shown via negative and positive signs of stream function, respectively.

Similar to uniform heating, streamlines show stronger convection for $\varphi = 45^\circ$ than that with $\varphi = 30^\circ$ and 0°. However, the strength of convection is less than that of uniform heating case.

At $Ra = 10^6, Da = 10^{-3}$ and $Pr = 7.2$, isotherms are compressed towards the side walls. The isotherms with $\theta \leqslant 0.4$ occur symmetrically near the side walls (Fig. 9). The isotherms are highly compressed near the bottom wall for all φ's (Fig. 9a–c). It is observed that $|\psi|_{max} = 12$ for all tilt angles which is greater than that at $Da = 10^{-5}$.

Comparative study for two limits of Prandtl numbers ($Pr = 0.026$ and $Pr = 988.24$) is shown in Figs. 10 and 11. Similar to uniform heating case, the stronger effect on convection occurs for $Pr = 988.24$. The boundary layer thickness is much reduced for $Pr = 988.24$ compared to $Pr = 0.026$. However, temperature gradient within the boundary layer is less compared with uniform heating. It may be noted that $\theta = 0.1$—0.5 are confined within the boundary layer for uniform heating case whereas $\theta = 0.1$—0.4 are confined within the boundary layer for non-uniform heating case for $Pr = 988.24$ with all tilt angles. It may also be noticed that the strength of convection is less in non-uniform heating case. It may be noted that for all tilt angles, $|\psi|_{max} = 15$ uniform heating case (Fig. 7) whereas $|\psi|_{max} = 13$ non-uniform case (Fig. 11). The streamlines are almost trapezoidal near the walls for high $Pr(Pr = 988.24)$ which was also observed even for uniform heating case.

4.4. Heat transfer rates: local and average Nusselt numbers

Fig. 12 shows the effects of tilt angles (φ), for salt water ($Pr = 7.2$) on the local heat transfer rates or Nusselt numbers at the bottom and side walls (Nu_b, Nu_s). Fig. 12a illustrates local Nusselt number distribution at the bottom wall (Nu_b) for $Ra = 10^6$ and $Da = 10^{-3}$. As a result of symmetry in the temperature field, heat transfer at the bottom wall is symmetric with respect to the mid-length ($X = 1/2$). Common to all cases ($\varphi = 0$—45°) with uniform heating, the temperature contours are widely dispersed at the center of the bottom wall and therefore local Nusselt number has a minimum at $X = 1/2$ for all φ's. The left inset plot within a distance 0.1—0.3 along the bottom wall shows that heat transfer rate is higher for $\varphi = 0^\circ$ than that for $\varphi = 45^\circ$ and $\varphi = 30^\circ$ with uniform heating.

The non-uniform heating provides a sinusoidal type of local heat transfer rate symmetric with respect to mid-length $X = 1/2$ and shows also a minimum value of Nu_b at $X = 1/2$ and edges. Two maxima in Nu_b is obtained at $X = 0.4$ and 0.6. This is due to fact that the circulations locally compress the isotherms at $X = 0.4$ and $X = 0.6$ due to non-uniform heating. It may be noted that, the local Nusselt numbers are found to be almost identical irrespective of φ's. The right inset plot illustrates Nu_b distributions for non-uniform heating. The increasing trend of Nu_b is observed

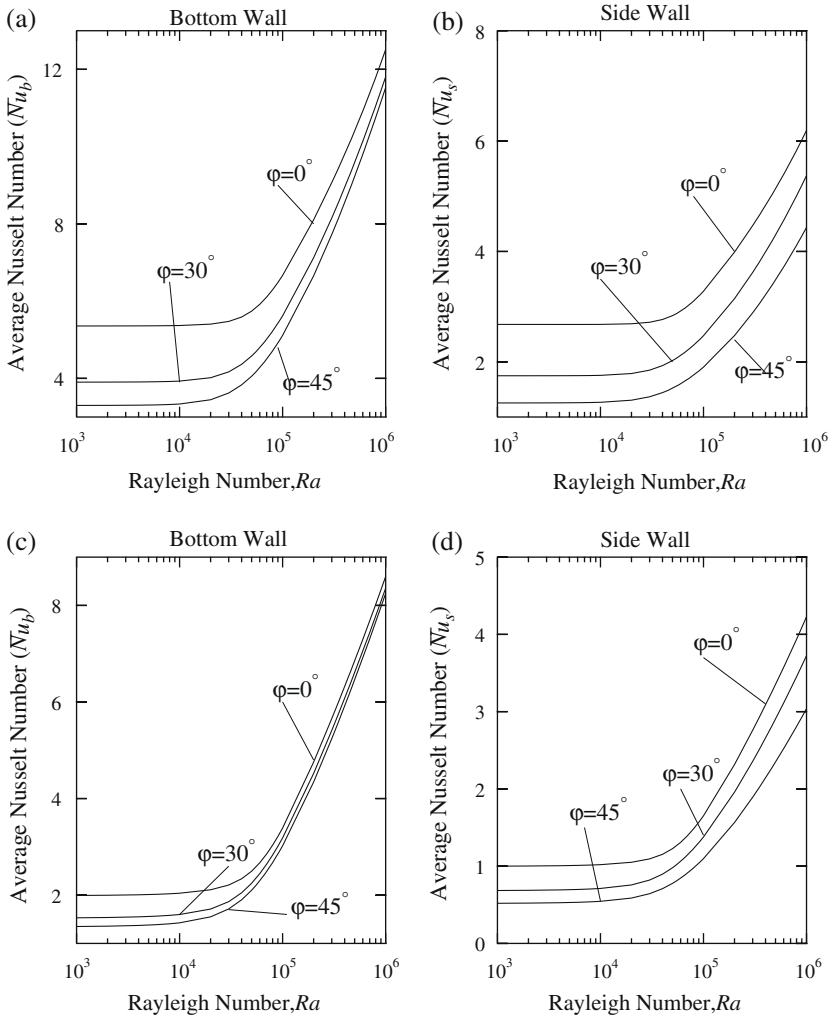

Fig. 13. Variation of average Nusselt number with Rayleigh number for $Pr = 7.2$ (salt water) and $Da = 10^{-3}$ for uniform heating (a) and (b) and non-uniform heating (c) and (d).

Table 1
Correlations for average Nusselt number for $Pr = 7.2$ and $Da = 10^{-3}$.

φ	$\overline{Nu_b}$		$\overline{Nu_s}$	
	Uniform heating	Non-uniform heating	Uniform heating	Non-uniform heating
45°	$0.2885Ra^{0.2592}$	$0.0437Ra^{0.3746}$	$0.1079Ra^{0.2603}$	$0.0181Ra^{0.3648}$
30°	$0.4469Ra^{0.2292}$	$0.0591Ra^{0.3533}$	$0.1932Ra^{0.2319}$	$0.0263Ra^{0.3521}$
0°	$1.0006Ra^{0.1746}$	$0.1112Ra^{0.3073}$	$0.5065Ra^{0.1727}$	$0.0574Ra^{0.3032}$

irrespective of φ and Nu_b at $\varphi = 0^\circ$ is slightly larger within $0.1 \leqslant X \leqslant 0.3$.

Heat transfer rates for uniform and non-uniform heating at the side walls are shown in Fig. 12b. At the bottom corner points, Nu_s is larger due to discontinuity in temperature for uniform heating case whereas due to dispersed isotherms or lower thermal gradients, the heat transfer rate for non-uniform case is lower than that for uniform heating case irrespective of Pr, Da and φ. At $Ra = 10^6$ and $Da = 10^{-3}$, the heat transfer rates for $\varphi = 0^\circ$ are larger except at the bottom corner points due to uniform heating as can be observed from the inset plot. It may be noted that, Nu_s increases with the vertical distance except near the top corner point for all φ. The larger thickness of the boundary layer at the top corner point leads to smaller Nu_s. The qualitative trend of Nu_s for non-uniform heating is similar to that with uniform heating.

The local heat transfer rates were also computed for olive oil ($Pr = 988.24$) and the qualitative trends obtained are similar to those for salt water ($Pr = 7.2$).

4.5. Overall heat transfer rate and average Nusselt numbers

The overall heat transfer rates for the sample fluid (salt water: $Pr = 7.2$) with various angles are displayed in Fig. 13a–d, where the distributions of the average Nusselt number of bottom and side walls, are plotted vs the logarithmic Rayleigh number. The average Nusselt numbers are obtained using Eqs. (14)–(16) where the integral is evaluated using Simpson's 1/3 rule. Fig. 13a and b illustrates uniform heating cases and Fig. 13c and d illustrates non-uniform heating cases. The average Nusselt numbers are found to be higher for $\varphi = 0^\circ$ than that for $\varphi = 45^\circ, 30^\circ$ along the bottom and side walls of the enclosure. The average Nusselt numbers for non-uniformly heated bottom wall (Fig. 13c and d) are very close for $\varphi = 45^\circ, 30^\circ, 0^\circ$ and the effect of the angle φ has less significance. The values of the average Nusselt numbers along the side walls are less compared to the bottom wall irrespective of the tilt angle φ. This is due to the fact that the length of the bottom hot wall is lower than the length of side or cold walls and also based on overall heat balance; $\overline{Nu_b} \times l_b = 2\overline{Nu_s} l_s$, where l_b= length of the bottom wall and l_s= length of the side walls.

The average Nusselt numbers show that the overall heat transfer rate decreases with increase in angle for most of the cases. It may also be noted that average Nusselt number increases with Ra for convection dominated heat transfer. The conduction dominant regime is shown as asymptotes in Fig. 13. The correlations for Nusselt number as function of Rayleigh number within convection dominated regime for various angles $\varphi = 45^\circ, 30^\circ$ and 0° are shown in Table 1. It may be noted that the convection dominant heat transfer is observed at high Darcy number ($Da = 10^{-3}$) whereas average Nusselt numbers do not vary significantly with Ra for lower Darcy number ($Da = 10^{-5}$) irrespective of Ra.

5. Conclusion

Role of uniform and non-uniform heating of the bottom wall and heat transfer characteristics due to natural convection flow in the porous trapezoidal enclosure has been studied. The penalty finite element method has been used and smooth solutions are obtained in terms of stream function and isotherm contours for wide ranges of Pr, Ra and Da. Numerical simulations were performed for molten metal ($Pr = 0.026$), salt water ($Pr = 7.2$) and olive oil ($Pr = 988.24$) with various values of Rayleigh numbers and Darcy numbers in the range $10^3 \leqslant Ra \leqslant 10^6$ and $10^{-5} \leqslant Da \leqslant 10^{-3}$ including side wall inclination angle $\varphi = 45^\circ, 30^\circ$ and 0° (square). At low Da, the heat transfer is mostly due to conduction irrespective of Ra and Pr. As Darcy number increases, the isotherms are highly compressed near the bottom and side walls for $Ra = 10^6$. The intensity of circulation also increases as Darcy number increases. Increase in the intensity of circulations and larger temperature gradients are observed with increase in φ from 0° to 45° especially at larger Pr and Ra. However, the strength of convection is lower for the non-uniform heating case as compared to uniform heating. It may also be remarked that the larger intensity of circulations for higher Pr fluid (olive oil) causes the shapes of stream functions to be almost trapezoidal near the walls and this signifies enhanced mixing effects.

The heat transfer effects are analyzed with local and average Nusselt numbers. It may be noted that, Nu_b for $\varphi = 45^\circ$ and $\varphi = 30^\circ$ are found to be identical whereas they are slightly larger for $\varphi = 0^\circ$ at $Ra = 10^6$ except near the corner points for uniform heating. It may be observed that Nu_b is larger at $0.25 \leqslant X \leqslant 0.75$ irrespective of φ's for non-uniform heating. On the other hand, Nu_s is largest for $\varphi = 0^\circ$ throughout the wall except the bottom corner point for uniform heating. Due to dispersed temperature contours or lower thermal gradients, the heat transfer rate for non-uniform heating is lower than that for uniform heating irrespective of Pr, Da and φ. However, Nu_s for non-uniform heating follows similar qualitative trends to that for uniform heating. It may be observed that the average Nusselt numbers are higher for $\varphi = 0^\circ$ compared to $\varphi = 45^\circ, 30^\circ$ along the bottom and side walls of the enclosure. The average Nusselt number for bottom wall during non-uniform heating is almost invariant with respect to φ for higher Ra. The values of the average Nusselt numbers along the side walls are less compared to the bottom wall irrespective of the tilt angle φ. Finally, the correlations between average Nusselt number and Rayleigh numbers are presented for the convection dominant regime.

Appendix A

The name 'iso-parametric' derives from the fact that the same parametric function describing the geometry may be used for interpolating spatial variable within an element. Fig. 2 shows a trapezoidal domain mapping to a square domain. The transformation between (x, y) and (ξ, η) coordinates may be defined via following relationship:

$$X = \sum_{k=1}^{9} \Phi_k(\xi, \eta) x_k \quad \text{and} \quad Y = \sum_{k=1}^{9} \Phi_k(\xi, \eta) y_k$$

where (x_k, y_k) are the X, Y coordinates of the k nodal points as seen in Fig. 2a and b and $\Phi_k(\xi, \eta)$ is the basis function. The nine basis functions are:

$$\Phi_1 = (1-3\xi+2\xi^2)(1-3\eta+2\eta^2)$$
$$\Phi_2 = (1-3\xi+2\xi^2)(4\eta-4\eta^2)$$
$$\Phi_3 = (1-3\xi+2\xi^2)(-\eta+2\eta^2)$$
$$\Phi_4 = (4\xi-4\xi^2)(1-3\eta+2\eta^2)$$
$$\Phi_5 = (4\xi-4\xi^2)(4\eta-4\eta^2)$$
$$\Phi_6 = (4\xi-4\xi^2)(-\eta+2\eta^2)$$
$$\Phi_7 = (-\xi+2\xi^2)(1-3\eta+2\eta^2)$$
$$\Phi_8 = (-\xi+2\xi^2)(4\eta-4\eta^2)$$
$$\Phi_9 = (-\xi+2\xi^2)(-\eta+2\eta^2)$$

The above basis functions are used for mapping the trapezoidal domain into square domain and the evaluation of integrals of residuals.

References

[1] M. Prud'homme, S. Jasmin, Inverse solution for a biochemical heat source in a porous medium in the presence of natural convection, Chem. Eng. Sci. 61 (2006) 1667–1675.

[2] L.B. Wang, N.I. Wakayama, Control of natural convection in non- and low-conducting diamagnetic fluids in a cubical enclosure using inhomogeneous magnetic fields with different directions, Chem. Eng. Sci. 57 (2002) 1867–1876.

[3] D. Hirsch, A. Steinfeld, Radiative transfer in a solar chemical reactor for the co-production of hydrogen and carbon by thermal decomposition of methane, Chem. Eng. Sci. 59 (2004) 5771–5778.

[4] Z.G. Du, E. Bilgen, Natural convection in vertical cavities with internal heat generating porous medium, Warme Stoffubertrag. 27 (1992) 149–155.

[5] T. Basak, S. Roy, A.R. Balakrishnan, Effects of thermal boundary conditions on natural convection flows within a square cavity, Int. J. Heat Mass Transfer 49 (2006) 4525–4535.

[6] O. Laguerre, S.B. Amara, D. Flick, Experimental study of heat transfer by natural convection in a closed cavity: application in a domestic refrigerator, J. Food Eng. 70 (2005) 523–537.

[7] M.M. Al-Hazmy, Analysis of coupled natural convection–conduction effects on the heat transport through hollow building blocks, Energy Buildings 38 (2006) 515–521.

[8] D. Jain, G.N. Tiwari, Effect of greenhouse on crop drying under natural and forced convection. I: Evaluation of convective mass transfer coefficient, Energy Convers. Manage. 45 (2004) 765–783.

[9] A. Omri, Numerical investigation on optimization of a solar distiller dimensions, Desalination 206 (2007) 373–379.

[10] A. Nakano, H. Ozoe, S.W. Churchill, Numerical computation of natural convection for a low-Prandtl-number fluid in a shallow rectangular region heated from below, Chem. Eng. J. 71 (1998) 175–182.

[11] T. Basak, S. Roy, S.K. Babu, A.R. Balakrishnan, Finite element analysis of natural convection flow in a isosceles triangular enclosure due to uniform and non-uniform heating at the side walls, Int. J. Heat Mass Transfer 51 (2008) 4496–4505.

[12] A. Bejan, D. Poulikakos, The nonDarcy regime for vertical boundary layer natural convection in porous medium, Int. J. Heat Mass Transfer 27 (1984) 717–722.

[13] D.A. Nield, A. Bejan, Convection in Porous Media, second ed., Springer, New York, 1999.

[14] D.B. Ingham, I. Pop, Transport Phenomena in Porous Media, Pergamon, 1998.

[15] D. Poulikakos, A. Bejan, B. Selimos, K.R. Blake, High Rayleigh number convection in the fluid overlaying a porous bed, Int. J. Heat Mass Transfer 7 (1986) 109–116.

[16] A.A. Merrikh, A.A. Mohamad, Non-Darcy effects in buoyancy driven flows in an enclosure filled with vertically layered porous media, Int. J. Heat Mass Transfer 45 (2002) 4305–4313.

[17] T.W. Tong, E. Subramanian, A boundary layer analysis for natural convection in vertical porous enclosures: use of Brinkman-extended Darcy model, Int. J. Heat Mass Transfer 28 (1985) 563–571.

[18] G. Lauriat, V. Prasad, Natural convection in a vertical porous cavity: a numerical study for Brinkman-extended Darcy formulation, Trans. ASME J. Heat Transfer 109 (1987) 688–696.

[19] H.C. Brinkman, On the permeability of media consisting of closely packed porous particles, Appl. Sci. Res. 1 (1949) 81–86.

[20] K. Vafai, C.L. Tien, Boundary and inertia effects on flow and heat transfer in porous media, Int. J. Heat Mass Transfer 24 (1981) 195–203.

[21] D. Poulikakos, A. Bejan, The departure from Darcy flow in natural convection in a vertical porous layer, Int. J. Heat Mass Transfer 28 (1985) 3477–3484.

[22] G. Lauriat, V. Prasad, Non Darcian effects on natural convection in a vertical porous enclosure, Int. J. Heat Mass Transfer 32 (1989) 2135–2148.

[23] R.A. Bortolozzi, J.A. Deiber, Comparison between two- and one-field models for natural convection in a porous media, Chem. Eng. Sci. 56 (2001) 157–172.

[24] I.A. Badruddin, Z.A. Zainal, P.A.A. Narayana, K.N. Seetharamu, Thermal non-equilibrium modeling of heat transfer through vertical annulus embedded with porous medium, Int. J. Heat Mass Transfer 49 (2006) 4955–4965.

[25] N.H. Saeid, I. Pop, Viscous dissipation effects on free convection in a porous cavity, Int. Commun. Heat Mass Transfer 31 (2004) 723–732.

[26] T. Basak, S. Roy, T. Paul, I. Pop, Natural convection in a square cavity filled with a porous medium: effects of various thermal boundary conditions, Int. J. Heat Mass Transfer 49 (2006) 1430–1441.

[27] A.C. Baytas, I. Pop, Natural convection in a trapezoidal enclosure filled with a porous medium, Int. J. Eng. Sci. 39 (2001) 125–134.

[28] I.E. Sarris, I. Lekakis, N.S. Vlachos, Natural convection in a 2D enclosure with sinusoidal upper wall temperature, Numer. Heat Transfer Part A Appl. 42 (5) (2002) 513–530.

[29] J.N. Reddy, An Introduction to the Finite Element Method, McGraw-Hill, New York, 1993.

[30] T.J. Chung, Computational Fluid Dynamics, Cambridge University Press, London, 2002.

[31] G.K. Batchelor, An Introduction to Fluid Dynamics, Cambridge University Press, 1993.

[32] E. Natarajan, T. Basak, S. Roy, Natural convection flow in a trapezoidal enclosure with uniform and non-uniform heating of bottom wall, Int. J. Heat Mass Transfer 51 (2008) 747–756.

[33] M.M. Ganzarolli, L.F. Milanez, Natural convection in rectangular enclosures heated from below and symmetrically cooled from the sides, Int. J. Heat Mass Transfer 38 (1995) 1063–1073.